Ore Geology Reviews 106 (2019) 1–11

Contents lists available at ScienceDirect

Ore Geology Reviews

journal homepage: www.elsevier.com/locate/oregeorev

Antimony in rutile as a pathfinder for orogenic gold deposits

Andrea Agangi[a,b,*], Steven M. Reddy[a], Diana Plavsa[a], Denis Fougerouse[a], Chris Clark[a], Malcolm Roberts[c], Tim E. Johnson[a]

[a] School of Earth and Planetary Sciences, Curtin University, Bentley 6102, Australia
[b] Department of Geology, University of Johannesburg, Auckland Park 2006, South Africa
[c] Centre for Microscopy Characterisation and Analysis, University of Western Australia, Crawley 6009, Australia

ARTICLE INFO

Keywords:
Gold
Antimony
Orogenic gold deposit
Indicator mineral
Exploration

ABSTRACT

In our study we explore the applicability of rutile as a pathfinder for orogenic gold deposits, which are an important source of this metal worldwide. We analysed rutile associated with orogenic Au deposits from three different Precambrian terranes, the Capricorn Orogen, the Barberton Greenstone Belt and the Ashanti Belt, all of which formed under greenschist conditions and share similarities in the style of mineralisation. Microtextural evidence from scanning electron microscopy and electron back-scatter diffraction indicates that rutile formed during the main deformation and alteration stage in these rocks, and is therefore related to mineralisation. We used electron microprobe and laser ablation ICP-MS to investigate the trace element compositions of rutile and we compared our results to other gold deposits. We find that hydrothermal rutile from gold deposits contains certain trace element characteristics, in particular high Sb concentrations (up to ~1500 ppm in Au deposits of the Capricorn Orogen), that are distinct from rutile from non-mineralised rocks of various petrogenetic origin. Other elements, such as W and Sn, are found to be more enriched in rutile from other rock types, namely felsic magmatic rocks and hydrothermal veins, and are therefore not diagnostic of Au mineralisation in this type of deposits. We also find that the presence of sub-μm-scale inclusions – in particular Zr-(Si, Th)-bearing phases, sulfide minerals and native Au – can severely affect analyses of this type of rutile and compromise the applicability of Zr-in-rutile geothermometry.

1. Introduction

A major challenge for the minerals industry lies in securing the necessary ore resources to respond to an ever increasing demand (Herrington, 2013). A promising approach to mineral exploration in rocks that are thickly-covered by regolith is the use of refractory accessory phases that can preserve indications of the mineralising process in their chemical composition, even after weathering and erosion of their host rocks. Although present only as a minor constituent of ore deposits, accessory minerals are concentrated during transport and deposition of sediments due to their high density. Many precious and base metals are associated with sulfide minerals, which are readily oxidised and thus rarely preserved in highly weathered rocks and in the sedimentary record (Fig. 1). However, other minerals, such as apatite, magnetite, zircon, titanite and rutile, are much more physically and chemically robust and have been proposed as indicators of ore forming processes (Belousova et al., 2002; Cao et al., 2012; Mao et al., 2016; Wilson and Cesbron, 1977). The successful application of such indicator minerals is dependent on finding a characteristic chemical signature that can unequivocally fingerprint a particular ore deposit type.

Rutile, the most abundant polymorph of titanium dioxide (TiO_2), is a common accessory mineral in fractionated felsic igneous rocks such as granites and pegmatites (Carruzzo et al., 2006; Černý et al., 1999; Plavsa et al., 2018) and in magmatic-hydrothermal ore systems such as porphyry Cu-Au deposits (Rabbia et al., 2009; Wilson and Cesbron, 1977). It is also a common constituent of metamorphic rocks, including skarns, ranging in grade from eclogite to greenschist facies (Liou et al., 1998), where it can form as a replacement product of Ti-bearing oxides and silicates, such as ilmenite, titanite or biotite (Luvizotto and Zack, 2009; Scott, 2005; Yang, 1987). Studies of rutile associated with gold deposits (Clark and Williams-Jones, 2004; Scott, 2005) have highlighted that the concentration of some elements, such as W, Sn, V and Sb, are elevated in rutile from mineralised rocks relative to rutile in the surrounding unmineralised country rocks. In addition, rutile can yield valuable constraints on the geological evolution of a region: Zr contents constrain magmatic/metamorphic temperatures (Zack et al., 2004), U-Pb isotopes provide absolute age determinations (Vry and Baker, 2006) and Cr–Nb systematics are used in provenance analysis (Meinhold et al.,

* Corresponding author.
E-mail address: aagangi@uj.ac.za (A. Agangi).

https://doi.org/10.1016/j.oregeorev.2019.01.018
Received 9 May 2018; Received in revised form 12 January 2019; Accepted 21 January 2019
Available online 22 January 2019
0169-1368/

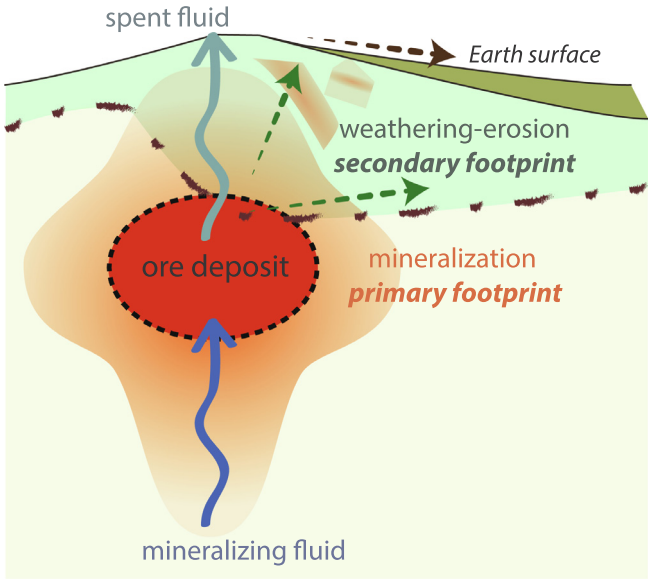

Fig. 1. Conceptual model of an ore deposit and its footprint. Metal-bearing mineralising fluids and the metal-depleted remainder of these fluids after ore deposition (spent fluids) leave a primary footprint in the form of characteristic minerals and elements in the rocks surrounding the ore. Dispersion of these minerals and elements related to weathering and erosion (dashed arrows in the figure) produces a secondary footprint that can be detected and explored by means of indicator minerals.

2008). The combined information means rutile has potential as a very powerful indicator mineral.

Here we present analyses of rutile associated with orogenic Au deposits, an important type of mineralisation that provide approximately a third of the world's reserves (Frimmel, 2008). The samples are from three areas of Precambrian terranes, the Capricorn Orogen in Western Australia, the Barberton Greenstone Belt in southern Africa, and the Ashanti Belt in western Africa. All areas host gold deposited from low-salinity aqueo-carbonic fluids under greenschist facies conditions and the distribution of the mineralisation is controlled by major crustal structures (i.e. orogenic gold (Mikucki and Ridley, 1993). The main aim of our study is to identify geochemical signals that can distinguish rutile from this type of Au deposits and non-mineralised rocks. We also discuss possible mechanisms of incorporation of impurities in rutile and then evaluate the applicability of the Zr-in-rutile geothermometer (Watson et al., 2006) to greenschist facies hydrothermal deposits.

2. Geological setting and samples

Samples were collected from mineralised zones at Fortnum, Killara and Nathans (Capricorn Orogen), Sheba and Fairview mines (Barberton Greenstone Belt), and Obuasi (Ashanti Belt). The geology of these deposits is briefly summarised below.

2.1. Capricorn Orogen: Padbury, Bryah and Yerrida groups

Samples representative of different small-scale structurally-controlled lode gold deposits and prospects hosted in the Palaeoproterozoic Padbury, Bryah and Yerrida groups of the Capricorn Orogen of Western Australia were used in this study. These basins developed between 2.0 and 1.8 Ga during collision of the Pilbara and Yilgarn cratons (Myers et al., 1996; Occhipinti et al., 2004). The lodes are hosted within high-strain zones affecting greenschist facies metasedimentary and metavolcanic rocks. The association of gold with quartz-carbonate veins is common to all the deposits, and hydrothermal alteration is characterized by quartz, muscovite, chlorite, biotite, carbonate, fluorite, tourmaline, pyrite (Pirajno et al., 2000; Thornett, 1995). The deposits are interpreted to have formed during retrogressive metamorphism (Pirajno, 2004).

Fluid inclusion studies from Peak Hill, Fortnum and Labouchere mines indicate that the mineralising fluids comprise both H_2O and CO_2, and had moderate salinity (7–12 wt% NaCl equivalent) (Windh, 1992). Microthermometry of these fluid inclusions yields homogenisation temperatures of 170–320 °C (Windh, 1992). In addition, alteration assemblages at Peak Hill indicate addition of Fe, K, S, B, F, CO_2, SiO_2 and H_2O (Thornett, 1995). Chlorite geothermometry indicates temperatures of 375 °C at Peak Hill (Thornett, 1995). Lead isotope measurements (Thornett, 1995; Windh, 1992) recalculated according to the Stacey and Kramers (1975) Pb evolution curve at Peak Hill, Nathans, Fortnum, Mt. Pleasant and Labouchere indicate mineralisation ages comprised between ca. 2.07 and 0.92 Ga (Hawke et al., 2015), suggesting deposition followed by remobilisation during different deformation events. The occurrence of rutile has been mentioned in deposits of the Peak Hill area, although only minor information is available (Thornett, 1995).

2.2. Barberton Greenstone Belt, Sheba and Fairview mines

The Palaeoarchaean Barberton Greenstone Belt is situated in the east of the Kaapvaal Craton, southern Africa. Its volcano-sedimentary succession, the ca. 3.55–3.22 Ga old Barberton (or Swaziland) Supergroup (Anhaeusser, 1973), is preserved in a southwest-northeast-trending belt surrounded by granitoid rocks, and has been subdivided into three main lithostratigraphic units: the mafic volcanic-dominated Onverwacht Group, and the sediment-dominated Fig Tree Group and Moodies Group, in stratigraphically ascending order (Viljoen and Viljoen, 1969). The Barberton Supergroup has been metamorphosed at greenschist to amphibolite facies conditions, with temperatures increasing towards the margins of the belt (Diener et al., 2005; Dziggel et al., 2005). Three major tectono-magmatic events have affected the northern terrane, located north of the Inyoka-Saddleback fault. The first and main event is related to accretion and collision of the southern and northern terranes at ca. 327 Ga (de Ronde and Kamo, 2000; Schoene et al., 2008), and coincided with emplacement of tonalite-trondhjemite-granodiorite (TTG) intrusions, such as the Kaap Valley Tonalite (Kamo and Davis, 1994).

All major greenschist-facies gold deposits in the Barberton Greenstone Belt occur as auriferous quartz-carbonate veins and sulfide bodies (Agangi et al., 2014; Anhaeusser, 1986). Ore assemblages include predominant pyrite and arsenopyrite, with minor chalcopyrite and sphalerite. Most gold is hosted by sulfides as "invisible" (or refractory) gold and microinclusions, whereas minor free-gold is associated with quartz veins (Cabri et al., 1989; de Ronde et al., 1992). Gold mineralisation is hosted by different rock types, ranging from metamafic-ultramafic rocks of the uppermost Onverwacht Group, to metasediments (greywacke, shale, sandstone) of the Fig Tree and Moodies groups.

Fluid inclusion studies from the major deposits hosted in greenschist facies rocks indicate predominant low-salinity (NaCl eq = 5–6 wt%), H_2O-CO_2-rich fluids, and homogenization temperatures in the T = 290–310 °C range (de Ronde et al., 1992). As-in-arsenopyrite estimates gave temperatures up to 400 °C (Agangi et al., 2014). Estimated mineralisation age ranges between 3,015 to 3,084 Ma, thus post-dating the main compressional stage in the greenstone belt by approximately 150 to > 200 Ma (de Ronde et al., 1992; Dirks et al., 2013; Dziggel et al., 2010). Rutile has been described at different mines as occurring in quartz-carbonate veins and in the mineralised host rocks (de Ronde et al., 1992).

2.3. Ashanti Belt, Obuasi

The Obuasi gold deposit is hosted in the Palaeoproterozoic (2.2–2.0 Ga) Birimian rocks of the west African craton, in the volcanosedimentary rocks of the Kumasi Basin (Kumasi Group) close to the

contact with the Ashanti volcanic greenstone belt (Sefwi Group). The Birimian rocks were metamorphosed to greenschist and amphibolite facies during the Eburnean orogeny between 2,125 to 1,980 Ma (John et al., 1999; Perrouty et al., 2012). The host rocks are mainly composed of phyllites, greywackes and volcano-sedimentary rocks.

The mineralisation in the Obuasi deposit is expressed in two mineralogically and temporally distinct types: (1) disseminated gold-bearing sulfides in metasedimentary rocks, and (2) overprinting native gold and sulfides in large quartz veins (Fougerouse et al., 2016b; Oberthür et al., 1998). The sulfide ores are composed of arsenopyrite, pyrite, pyrrhotite, marcasite, chalcopyrite, sphalerite and rare gold grains. Arsenopyrite is the main gold-bearing phase in the sulfide ores with concentration up to approximately 2200 ppm Au reported by atom probe microscopy (Fougerouse et al., 2016c). The overprinting quartz vein ore assemblage is composed of native gold but also minor abundance of galena, chalcopyrite, sphalerite, bournonite, boulangerite, tetrahedrite, aurostibine, löellingite, pyrite, arsenopyrite, and rare bismuth tellurides (Oberthür et al., 1998). Based on replacement textures and microstructural evidence, the quartz vein ores have been interpreted to be the product of gold remobilisation from the disseminated sulfide ores (Fougerouse et al., 2016a). In the Ashanti Belt, the mineral assemblage actinolite + chlorite + clinozoisite + quartz + calcite was estimated to have formed at temperatures of 340–460 °C and pressure of 2 kbar (Schwartz et al., 1992). Arsenic-in-arsenopyrite in Au-bearing arsenopyrite gave temperatures < 300–410 °C (Mumin et al., 1994).

Rutile is present both in the sedimentary rocks and quartz veins and has been interpreted to form early in the paragenetic sequence from destabilisation of ilmenite and magnetite (Schwartz et al., 1992). Hydrothermal rutile U-Pb dating from granite-hosted satellite deposits at 2098 ± 7 Ma indicate mineralisation to have occurred during the Eburnean orogeny (Oberthür et al., 1998).

2.4. Microtextures and microstructures of rutile

Samples from the Capricorn Orogen are sourced from mineralisation at Fortnum (samples FTD52 120.8 m and 110959), Killara (110944, 110945) and Nathans (114034) and are composed of foliated chlorite-quartz-carbonate-rich metasedimentary rocks with euhedral pyrite or magnetite. The foliation is defined by the orientation of chlorite and quartz-carbonate lensoid aggregates (Fig. 2). Rounded Cr-spinel grains occur as cores to euhedral magnetite in sample FTD52 120.8 m. Fe-Ca-Mg carbonate occurs in sample 110944 (Killara) as laths and cross-cutting veinlets, and chlorite-rich domains occur in interstitial positions between feldspar and quartz.

Samples of Barberton Greenstone Belt mineralisation were collected at Fairview (46CMR and 62-11) and Sheba (33ZKA and 33ZKB) mines. Sample 46CMR is a fine-grained foliated metagreywacke, mostly composed of oriented muscovite, quartz, Fe-Mg carbonate, and μm-scale anhedral monazite. Sample 62-11 is representative of sulfide mineralisation at the contact between chert and greywacke. Samples 33ZK-A and 33ZK-B include quartz-carbonate-sulfide veins in strongly deformed and silicified (ultra)mafic volcanic rocks and chert. Cr-spinel is present as an accessory mineral. Ore minerals include pyrite, chalcopyrite, ullmannite, gersdorffite, and sphalerite.

Samples 63089 and DF-H01, collected at Obuasi, Ashanti Belt, are representative of mineralised muscovite-quartz-ankerite-chlorite-graphite phyllite (Fougerouse et al., 2016b). Ore minerals include euhedral arsenopyrite, up to several mm in size, and interstitial pyrite. The rocks are complexly deformed and the main foliation, marked by muscovite, is folded; crenulation cleavage is well-developed (Fig. 2).

3. Analytic methods

3.1. TiO_2 polymorph identification and microstructural information

Titanium dioxide grains were studied by electron back-scatter diffraction (EBSD) analysis, which involves indexing observed diffraction patterns with theoretical reflector files, and allows both polymorph identification and lattice orientation. EBSD maps were collected by gathering multiple diffraction patterns along a grid of approximately 1 μm size. The TiO_2 polymorphs rutile, anatase and brookite can have different trace element compositions (Triebold et al., 2011). Therefore, it is important to identify the TiO_2 polymorph before comparing the compositional data from different TiO_2 grains. In this study, TiO_2 polymorphs were distinguished by EBSD (Taylor et al., 2012). As different TiO_2 phases may co-exist in single grains (Plavsa et al., 2018; Triebold et al., 2011), phase mapping is preferred to single-spot identification. In addition to phase identification, EBSD offers important microstructural information, such as the presence of sub-grain textures and the orientation of crystals with respect to the foliation (e.g. Reddy et al., 2007).

The EBSD acquisition parameters include voltage of 20 kV, spot size between 18 and 27 nm and working distances between 19 and 22 mm. Grain mapping was carried out at different step sizes (0.5–2 μm) depending on the map size, analytical resolution and time efficiency. Detailed information on the phase identification and match units used for the different TiO_2 polymorphs is given by Reddy et al. (2007) and Plavsa et al. (2018). The accuracy and validity of the method was achieved by maximizing the number of Kikuchi bands used for electron backscatter pattern (EBSP) indexing (8 bands used here). The accuracy of the analytical method is measured by the closeness of fit between the empirical and theoretical diffraction patterns, the mean angular deviation (MAD), with values < 1 suggesting a good fit. During the course of the analytical run, rutile yielded MAD values between 0.1 and 0.7 demonstrating the accuracy of the analytical method.

3.2. Microchemical analyses

Samples of rutile from gold deposits have been analysed by electron microprobe (EPMA) at the Centre for Microscopy Characterisation and Analysis at the University of Western Australia. Ilmenite and magnetite coexisting with rutile were also analysed for comparison. Analyses were performed by EPMA using a five spectrometer-equipped JEOL 8530F Hyperprobe. Analytical conditions were 25 kV accelerating voltage, 130 nA beam current and fully focused beam. The elements Ti, V, Cr, Sb, Si, As, Ca, Nb, Sn, Zr, Au, Mn, Hf, Fe, Ta, W were analysed. All elements have been analysed for 100 s, except Ti, analysed for 20 s. The Au (Lα line) was analysed on two spectrometers. Elements were calibrated on a suite of natural and synthetic silicate, oxide and metal standards. Data acquisition and reduction made use of the Probe for EPMA software. Mean Atomic Number background corrections were used following the methodology of (Donovan and Tingle, 1996). Unknown and standard intensities were corrected for deadtime and the ZAF algorithm utilised for matrix absorption (Armstrong, 1988). On peak interference corrections were applied as appropriate (Donovan et al., 1993). Detection limits are between ~20 ppm and ~70 ppm for most elements, apart from Ti and Sb (100–150 ppm), Sn (250 ppm). High Si concentrations (up to several wt% level) are indicative of contamination with quartz finely intergrown with rutile. While this contamination would have limited dilution effect on trace elements of interest to this study, analyses with the highest Si concentrations have been excluded from the dataset.

The analyses were compared with a dataset that includes rutile from high- and medium-temperature and high-pressure metamorphic rocks, granitoids from the Capricorn Orogen and other areas, and previous analyses of rutile from lode gold deposits. Previously published chemical analyses of rutile from various sources used for comparison were obtained from a combination of EPMA and LA-ICP-MS techniques. Data are from (Cabral et al., 2013; Černý et al., 1999; Clark and Williams-Jones, 2004; Dostal et al., 2009; Harris, 1989; Kotková and Harley, 2010; Liu et al., 2014; Luvizotto and Zack, 2009; Meinhold et al., 2008; Rice et al., 1998; Scott and Radford, 2007; Zack et al., 2002; Plavsa

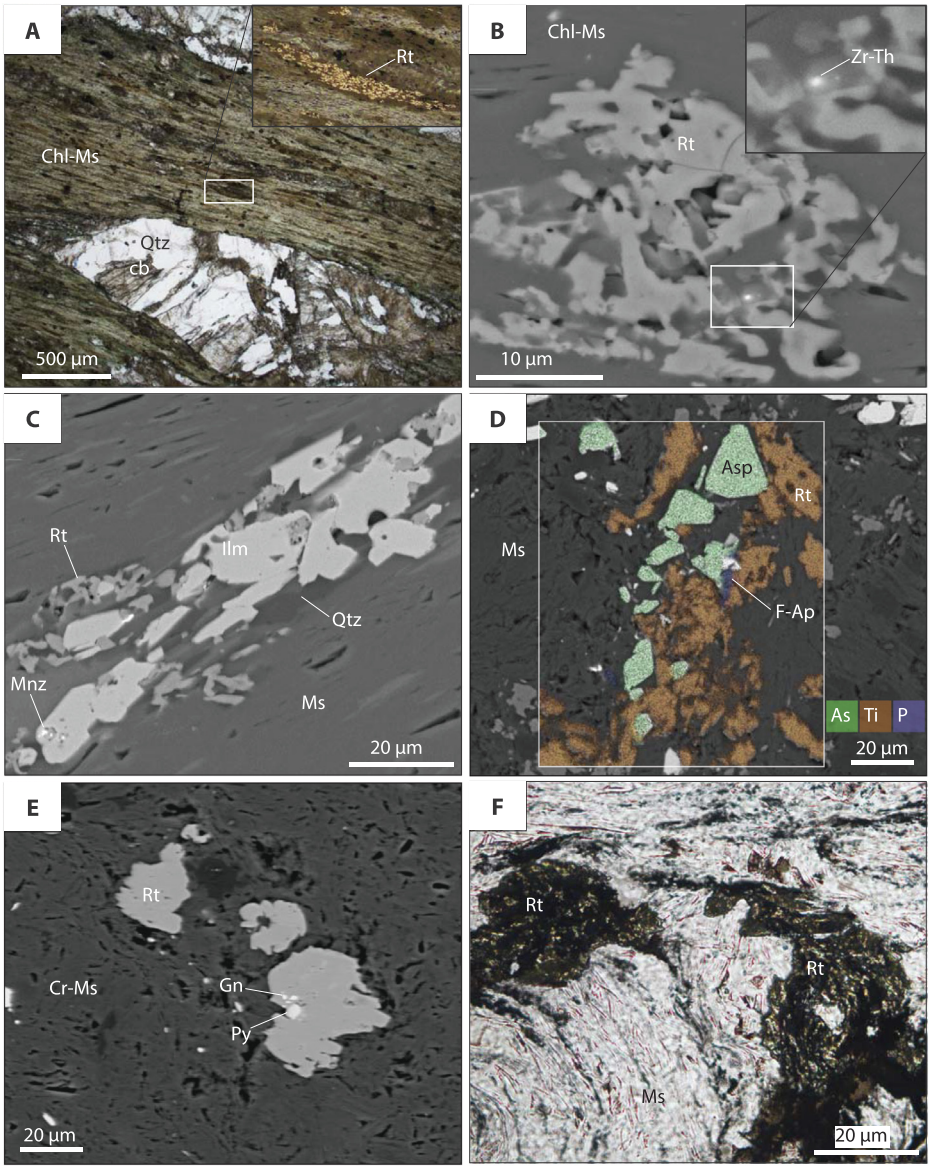

Fig. 2. Microtextures of rutile in gold-bearing samples from the Capricorn Orogen, Barberton Greenstone Belt and Ashanti Belt. A and inset. Muscovite-chlorite schist with lensoid aggregates of quartz and carbonate. Rutile is elongate parallel to foliation (inset). Plane polarised transmitted and reflected light, sample 110945, Killara (Capricorn Orogen). B and inset. Rutile intergrown with chlorite-muscovite matrix containing nano-scale grain of Zr and Th-bearing mineral. C Ilmenite overgrown by rutile aggregates. Note fine-grained monazite (< 1 µm). B and C BSE image, sample 110945, Killara. D Anhedral rutile associated with pyrite-arsenopyrite mineralisation and F-apatite. BSE image and XR element maps (As, Ti, P), sample 46CMR, Fairview mine (Barberton Greenstone Belt). E Rutile in Cr-muscovite matrix with µm-scale inclusions of sulfide minerals. BSE image, sample 33ZKA, Sheba mine. F Aggregates of fine-grained rutile along the foliation. Plane polarised transmitted light, sample 63098, Obuasi. Abbreviations: Asp arsenopyrite, cb carbonate, Chl chlorite, F-Ap fluorapatite, Gn galena, Hae hematite, Ilm ilmenite, Mag magnetite, Mnz monazite, Ms muscovite, Qtz quartz, Rt rutile.

et al., 2018). Further details on analytical settings can be found in these publications.

3.3. Chemical depth profiling

The distribution of trace elements and the presence of inclusions have been tested in time-resolved laser ablation inductively-coupled plasma mass spectrometry (LA-ICP-MS) spectra (depth-profiling). LA-ICP-MS trace element analyses were carried out using a Coherent CompEX 193 nm laser ablation system and an Agilent 7700 ICP-MS at the John de Laeter Centre, Curtin University. Ablation was performed at 7 Hz repetition rate, 50 µm spot size and 26% power (approximately 2–3 J/cm^2 fluence). During the analyses, 20 s of background acquisition were followed by 50 s of ablation. The following masses have been monitored: Mg^{24}, Al^{27}, Si^{28}, P^{31}, S^{34}, K^{39}, Ca^{43}, Ca^{44}, Ti^{47}, Ti^{49}, V^{51}, Cr^{53}, Mn^{55}, Fe^{56}, Fe^{57}, Co^{59}, Ni^{60}, Cu^{65}, Zn^{66}, Se^{77}, Zr^{90}, Nb^{93}, Mo^{95}, Ag^{107}, Sn^{118}, Sb^{121}, Te^{125}, Ta^{181}, W^{182}, Au^{197}, Tl^{205}, Pb^{206}, Pb^{207}, Pb^{208}, Bi^{209}. Each mass was analysed for 0.01–0.03 s (total sweep approximate time 0.5 s). Quantification of element concentrations was obtained using glass NIST 610 and assuming TiO_2 = 100 wt%.

4. Results

Samples were initially analysed by electron back-scattered diffraction (EBSD), which measures crystallographic orientation and allows rutile to be distinguished from other TiO_2 polymorphs, such as brookite and anatase. In all the samples, rutile is the only polymorph and occurs in elongate mineral aggregates oriented parallel to the foliation (Fig. 2) that are composed of rutile needles intergrown with quartz, chlorite, carbonate and Fe-(Ti)-oxide. In the Barberton samples, rutile aggregates are also associated with pyrite, arsenopyrite, F-apatite and muscovite (Fig. 2d). Rutile-hosted inclusions of sulfides and various Zr, Th and rare earth element-bearing minerals occur locally in the Capricorn and Barberton samples (Fig. 2). In samples from all the terranes analysed, pole figures of crystallographic c axes of rutile grains within the aggregates indicate three main alignments that have ~60° misorientation from each other, in which small deviations (< 10°) are accommodated by low-angle boundaries (Fig. 3).

The needles of rutile with ~60° misorientation (reticulated rutile) typically form by replacement of other Ti-bearing minerals, such as ilmenite, Ti-magnetite, biotite and titanite (Force, 1980; Rabbia et al., 2009) and have been synthetised in the laboratory during annealing experiments (Putnis, 1978). Formation of such reticulated rutile is

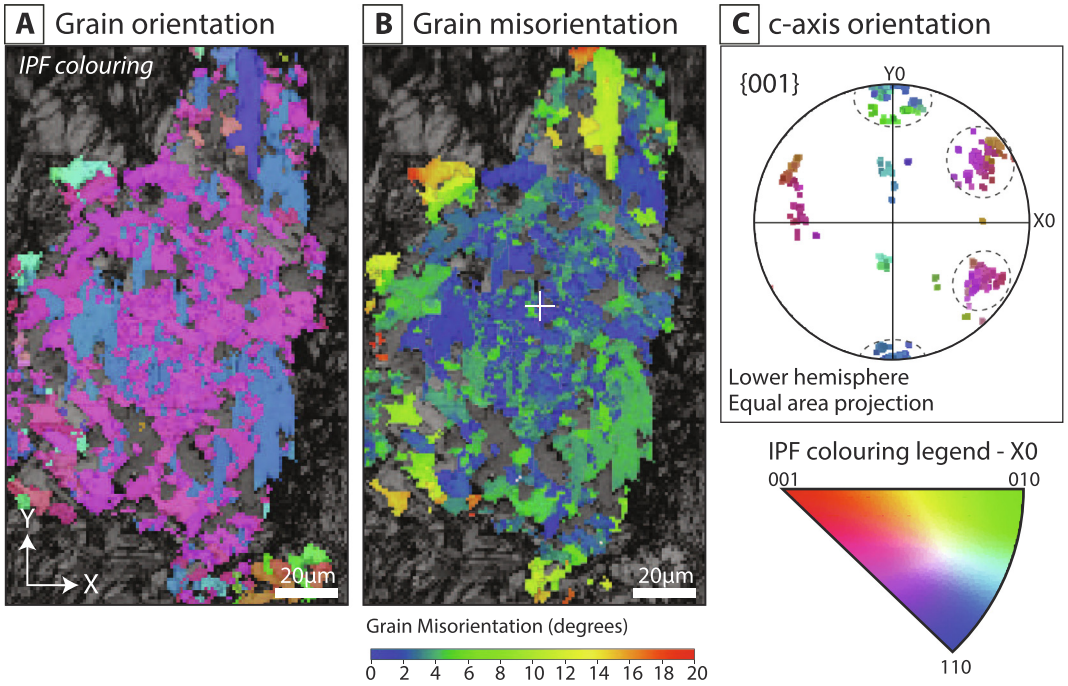

Fig. 3. EBSD-based crystallographic orientation diagram of rutile from gold deposits of the Capricorn Orogen. A Domains of rutile with similar crystallographic orientations. B Grain misorientation map. Note stronger misorientation (yellow-red) due to deformation at grain margin. C Plots of crystallographic c axes indicating three main clusters (dashed lines) at around 60° from each other.

typically accompanied by the development of microporosity due to removal of Fe and other elements from precursor minerals (Morad, 1986). The presence of ilmenite and fine-grained Fe-oxide, common in Capricorn samples, is also compatible with rutile formation by replacement of an ilmenite precursor. In our samples, rutile is intergrown with Fe-(Mg-Ca)-carbonate, quartz and chlorite, all of which have infilled micro-pores between rutile needles (Fig. 5). In the presence of CO_2, this replacement may occur due to the carbonate-forming reaction $FeTiO_3 + CO_2 = FeCO_3 + TiO_2$ (Yang, 1987). Formation of carbonate is compatible with the mineral assemblages of our samples, and with the alteration associated with orogenic gold deposits in general (Mikucki and Ridley, 1993).

In situ chemical analyses of rutile carried out using electron microprobe are shown in Fig. 4 and listed in Supplementary Table 1. Multiple spot analyses within single grains or grain aggregates indicate strong compositional variations for several different elements, most notably Nb, W, Zr and V. For instance, in a metasedimentary sample (46CMR, Barberton), Nb concentrations can vary from 400 ppm to 15,000 ppm within a single grain and Zr concentrations by more than an order of magnitude in single grain aggregates. In samples from Barberton, concentrations of Nb and Fe are positively correlated (Fig. 4), which suggests incorporation of these elements by coupled replacement of Ti according to the reaction $2Ti^{4+} = Nb^{5+} + Fe^{3+}$. Other samples have high and scattered Fe values that deviate from the 1:1 line in the Nb vs. Fe plot, likely due to contamination by fine-grained Fe-Ti-oxide phases that were observed in SEM images and X-ray element maps (Fig. 6). The concentrations of W range from detection limit (~60 ppm) to approximately 48,000 ppm (the highest values were measured in samples from the Ashanti Belt and the Capricorn Orogen), Sn concentrations are up to 6400 ppm in Barberton samples (but mostly < 800 ppm in samples from the Capricorn Orogen and Ashanti Belt). Antimony concentrations are up to ~1500 ppm. In LA-ICP-MS depth profiles, obtained by plotting signal intensity (counts per seconds, cps) versus analysis time (s), the Au signal intensity is discontinuous. Gold peaks coincide with S and the chalcophile elements (Ni and Co, Pb, Mo) (Fig. 7). This suggests that Au occurs in sulfide inclusions, rather than in the rutile structure. The signal of Sb is rather homogeneous throughout the ablation, suggesting incorporation in the structure of rutile or in nanoscale inclusions not resolvable with the LA-ICP-MS. In a few cases, however, Sb peaks coincide with Ni-(Co) peaks or with Pb-Bi peaks (Fig. 7), suggesting incorporation of additional Sb in sulfides such as ullmannite [NiSbS], and galena. Zirconium distribution is also very irregular, in agreement with the variable EPMA concentrations. In contrast, the ablation signals of Nb, Ta and W are relatively continuous and only show smooth variations, which suggests incorporation in the rutile structure.

5. Discussion

5.1. Geochemical comparison of rutile from Au-mineralised and unmineralised rocks

The observed microstructures have important implications on the timing of rutile formation. The low angle deformation features observed in EBSD images (Fig. 3c) indicate that rutile crystallised during deformation, and the intimate intergrowths with chlorite and carbonate suggest that it formed during the main alteration and mineralisation event. Therefore, we interpret the chemical composition of rutile to reflect the composition of gold-bearing mineralising fluids.

In order to identify elements that can distinguish rutile associated with orogenic gold deposits, we compared our analyses with a large geochemical dataset of rutile from metamorphic and igneous rocks and other gold deposits (Fig. 4). This comparison indicates that high contents of W, Sn and V are common, although not unique, in rutile from gold deposits. When plotted in the 100·(Fe + Cr + V) − Ti − 1000 W diagram (Clark and Williams-Jones, 2004), designed to discriminate between rutile from gold-mineralised and barren country rocks, analyses from different rock types largely overlap with the field of mineralised rutile (Fig. 4). Concentrations of Sn and W exceeding those presented here have been measured in granitoids, and high V concentrations were found in both granitoids and metamorphic rocks unrelated to mineralisation. Tungsten-Sn-rich rutile of felsic magmatic-hydrothermal origin could also be inherited by sediments deriving from erosion of igneous terranes. Indeed, destabilisation of W-rich detrital

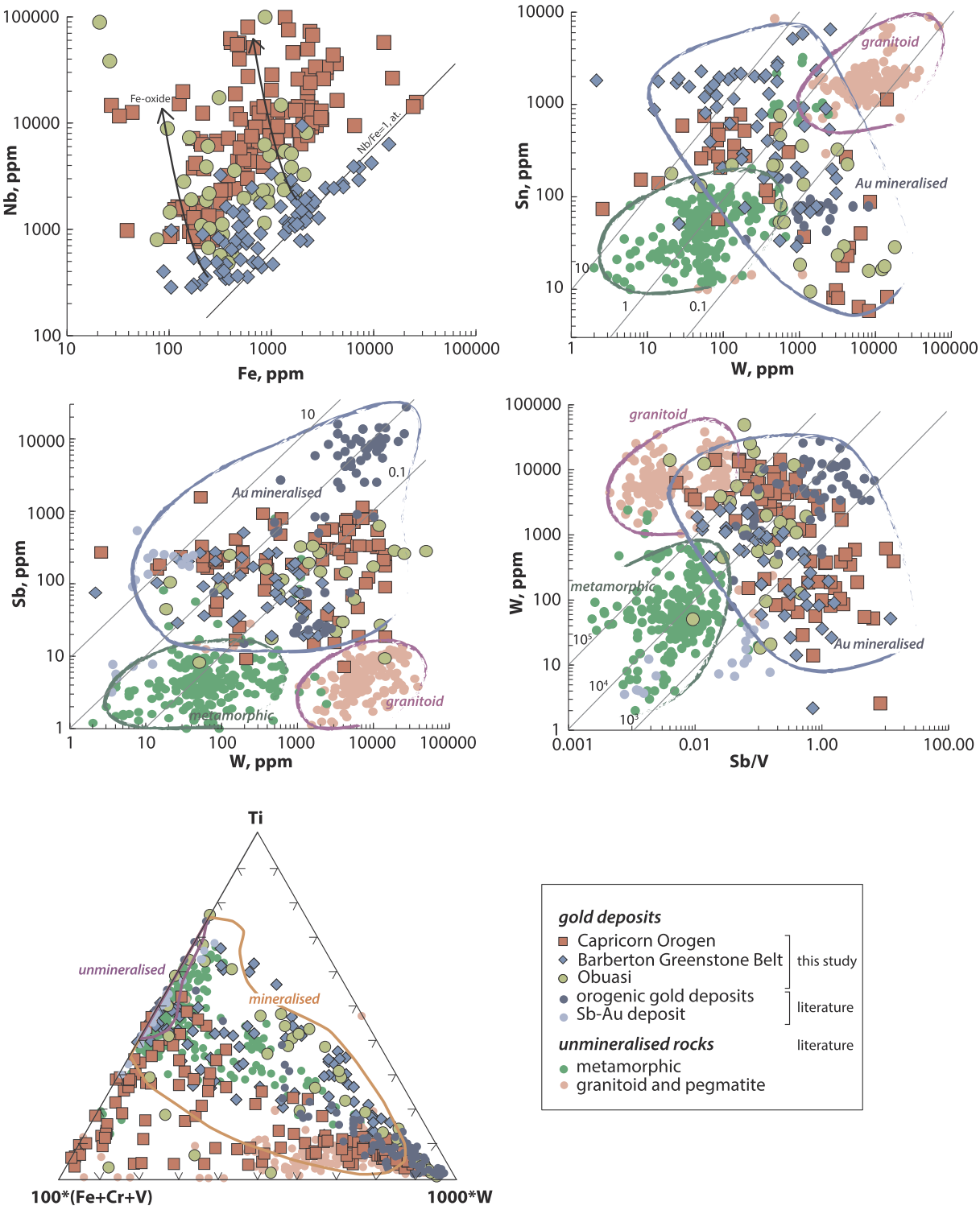

Fig. 4. Microchemical analyses (EPMA) of rutile from gold deposits and other unmineralised rocks. All elements plotted as parts per million (ppm), analyses reported in Additional Table1. Elements such as Sn and W cannot unequivocally fingerprint rutile from gold deposits, whereas Sb is an effective indicator of mineralisation. Plot of Ti-100*(Fe + Cr + V)-1000*W from (Clark and Williams-Jones, 2004). Literature analyses from various techniques; data for metamorphic rutile: Liu et al. (2014); Luvizotto and Zack (2009); Meinhold et al. (2008); Pape et al. (2016); Skublov et al. (2013); Smith and Perseil (1997); Zack et al. (2002); igneous rutile: Černý et al.(1999); Kotková and Harley (2010); Plavsa et al. (2018); lode Au: Clark and Williams-Jones (2004); Cabral et al. (2013); Dostal et al. (2009); Harris (1989); Scott and Radford (2007); Sb-Au deposit: Pochon et al. (2017).

rutile in sub-greenschist conditions has been proposed as the source of W in the orogenic Au-hosting Otago Schist of New Zealand (Cave et al., 2015).

Thus, high W, Sn and V concentrations alone are equivocal indicators of gold mineralisation, especially when studying detrital rutile, for which the nature of source rocks cannot readily be ascertained. This conclusion is only apparently in contrast with results of previous studies (e.g., Clark and Williams-Jones, 2004; Scott and Radford, 2007), who compared rutile from mineralised zones and the immediately adjacent barren rocks. This approach allows appreciation of mobility of trace

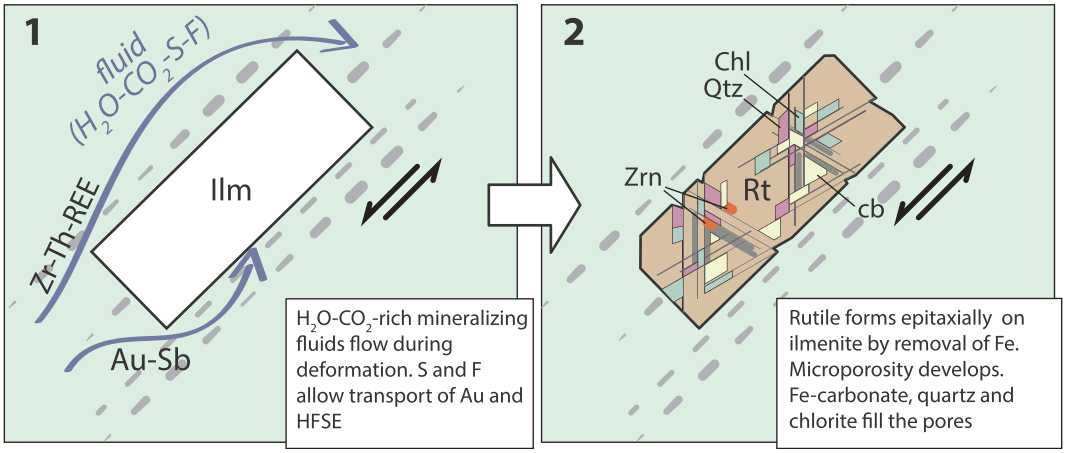

Fig. 5. Model of rutile formation via replacement of precursor Fe-Ti oxide. Flow of mineralising fluids (blue arrows) accompanies deformation (black arrows). Rutile develops at characteristic angles of approximately 60°. Porosity developed during removal of Fe is infilled by Fe-carbonate, quartz and chlorite. In addition to Au and Sb, mineralising fluids are also capable of mobilising scarcely soluble elements, such as high-field strength elements (HFSE: Zr, Th) and rare earth elements. Abbreviations: cb carbonate, Chl chlorite, Ilm ilmenite, Qtz quartz, Rt rutile, Zrn zircon.

elements during fluid flow and mineralisation in homogenous rock types, and may reflect transfer of some elements from country rocks to the ore zone. However, the broader approach adopted here allows minimising the misidentification of rutile as mineralisation-related (or "false positives"), and is more applicable to campaign-style greenfield exploration, where rutile from a wide variety of rocks may be targeted at once.

In contrast to W, Sn and V, Sb is higher in rutile from gold deposits

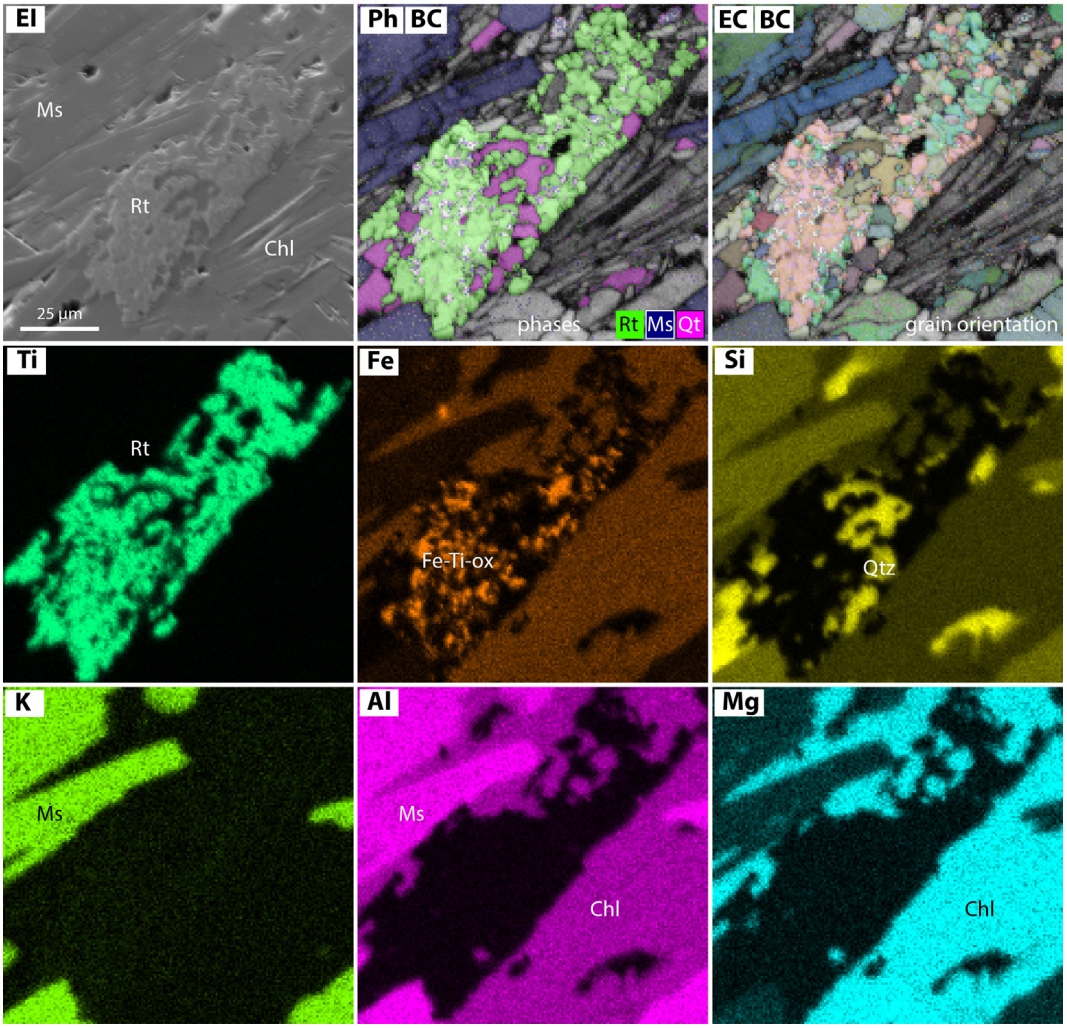

Fig. 6. Electron image, XR maps and EBSD maps of rutile from Fortnum. Sample FTD52-120.8. BC band contrast, Ph phase map, EC Euler color. Abbreviations: Chl chlorite, Qtz quartz, Ms muscovite, ox oxide, Rt rutile.

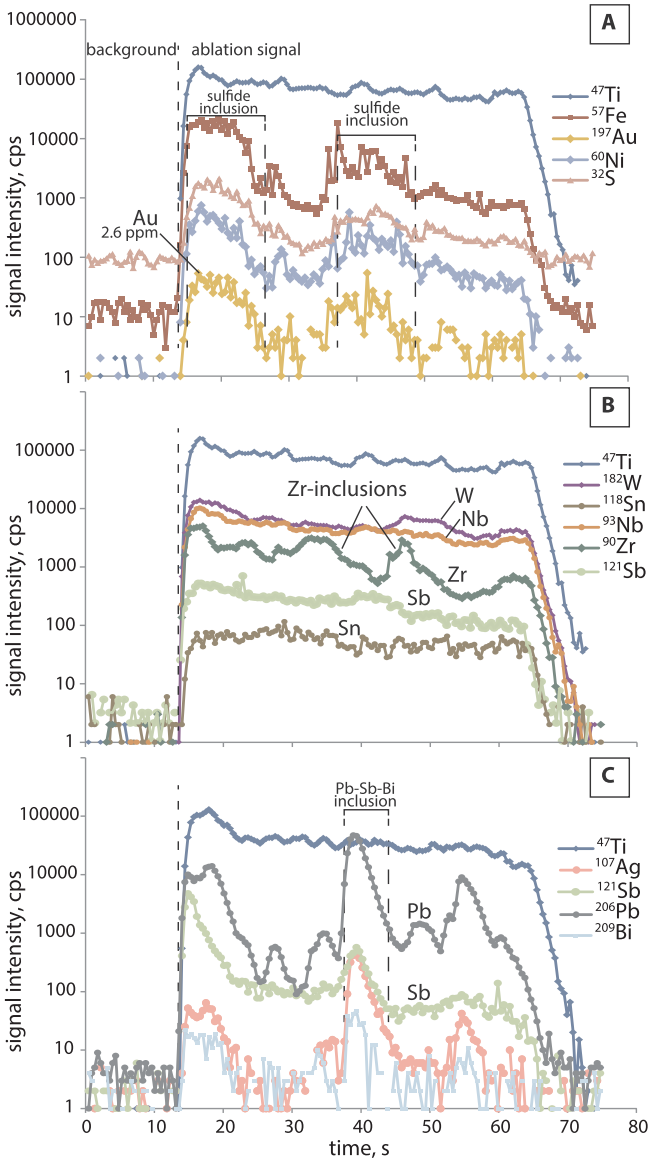

Fig. 7. Laser ablation ICP-MS spectra (depth profiles) of rutile from Sheba mine, Barberton Greenstone Belt (sample 33KZB-b). Spikes in specific elements indicate the presence of inclusions of sulfide minerals (e.g. S, Au, Mo) (A) and Zr-bearing minerals (C). Antimony has mostly flat signal (B) and is likely present in the structure of rutile or nanoinclusions, although spikes associated with Pb were also observed (C).

when compared with a wide variety of unmineralised rocks (Fig. 4). Even more pronounced Sb enrichments have been measured in rutile from gold deposits formed at higher temperature conditions (medium-grade metamorphism), such as Hemlo, Canada and Big Bell, Australia (Clark and Williams-Jones, 2004; Harris, 1989; Scott and Radford, 2007). Recent analyses of rutile associated with Sb-Au deposits hosted in greenschist facies metamafic rocks of the Variscan Armorican Massif, France (Pochon et al., 2017), have indicated strongly variable Sb concentrations in rutile that show bimodal distribution, and ranging from < 1 ppm (typical of unmineralised metamorphic rocks) to 540 ppm (typical of Au-mineralised rocks) (Fig. 4).

5.2. Mechanisms of incorporation of Sb into rutile

A recent atom probe investigation of rutile from amphibolite grade metamorphic rocks of the Capricorn Orogen (Verberne et al., 2017) provides useful indications on the mode of incorporation of some trace elements in rutile. These authors have detected nanoscale clusters of Pb interpreted as due to element mobilisation and trapping in crystal defects. The clusters have higher concentrations of Al, Cr, Sn and V in comparison with the surrounding rutile, whereas Nb, Sb, W and Zr show no variations. The homogeneous distribution of the latter elements suggests lack of mobility and is compatible with their incorporation in the mineral structure in this specific example.

The mode of incorporation of Sb^{5+} in the rutile structure can be informed by the behaviour of Nb^{5+} as indicated by its correlation with Fe^{3+}, and by the correlations between trivalent and pentavalent cations in general. The positive correlation between M^{5+} and M^{3+} (Fig. 4) suggests a coupled substitution of the type $M^{5+} + M^{3+} = 2Ti^{4+}$ (Smith and Perseil, 1997), where M^{5+} is a pentavalent cation, such as Nb^{5+} or Sb^{5+}, and M^{3+} is a trivalent cation, such as Fe^{3+}, Cr^{3+} or Al^{3+}. Arsenic may also be an important trivalent cation in rutile from orogenic gold deposits. Another possible replacement mechanism for M^{5+} includes $2M^{5+} + M^{2+} = 3Ti^{4+}$ (Smith and Perseil, 1997), which requires incorporation of divalent cations such as Mg^{2+}, Fe^{2+} or Ni^{2+}.

The virtually identical ionic radius of Sb^{5+} and Ti^{4+} (both 60 pm; Shannon, 1976) is arguably favourable for the replacement of Ti^{4+} in the rutile structure, provided that charge balance can be ensured. This requirement implies that the incorporation of Sb into rutile will be partly controlled by the behaviour of the coupled substitution. The most abundant trivalent cations in rutile (Al^{3+}, Cr^{3+}, Mn^{3+}, Fe^{3+}) have effective ionic sizes ranging between 54 (for Al^{3+}) and 64 pm (for Fe^{3+} at high spin state), so that the incorporation of the relatively large cations will be favoured by increasing temperatures. This may be partly explain the high Sb concentrations in amphibolite facies gold deposits, such as Hemlo (Scott and Radford, 2007). Trivalent Sb^{3+} has much larger ionic radius of 76 pm and is not considered to be a likely replacement for Ti^{4+} in rutile (Smith and Perseil, 1997). In addition to these mechanisms, non-equilibrium incorporation of trace elements during fast mineral growth should also be taken into consideration, especially in hydrothermal environments, and will be considered in the following discussion.

5.3. Disequilibrium crystallisation and implications on Zr-in-rutile geothermometry to greenschist facies hydrothermal rocks

The application of the geothermometer based on Zr content in rutile (Tomkins et al., 2007) to samples from the three studied areas gives broadly overlapping temperatures up to 674 °C (at the relevant pressure of 2 kbar), with outliers up to 815 °C (Fig. 8). These estimates far exceed independent maximum temperature estimates, which range from 375 °C in the Capricorn Orogen to ≤460 °C for the Ashanti Belt (Agangi et al., 2014; Schwartz et al., 1992; Thornett, 1995) and imply that equilibrium was not reached. The thermometer is based on the requirement of equilibrium between rutile, zircon and quartz, a condition that can be met in slowly heating and cooling regional metamorphic rocks, especially when element diffusion is favoured at medium to high temperatures. In contrast, rutile from orogenic Au deposits formed during rapid hydrothermal events that are typically characterised by pulsating fluid flow and at relatively cool temperatures (Jiang et al., 1997; Sibson et al., 1988). These characteristics are recorded by the zoning of minerals and by truncation and recrystallisation textures (Agangi et al., 2016; Mumin and Fleet, 1995). The transient nature of these processes helps explain why the Zr-in-rutile thermometer yielded improbable results in our samples. Incorporation of Zr as nanoscale inclusions (Fig. 2) helps explain the mismatch between Zr-in-rutile and other types of geothermometry, which has been previously observed in hydrothermal rutile (Cabral et al., 2015). Some of these inclusions are too small to be individually analysed by EPMA or LA-ICP-MS, but the correlation of Zr and Si in some analyses suggests the presence of zircon [$ZrSiO_4$]. Some high-Zr analyses do not contain Si, likely due to the presence of baddeleyite [ZrO_2], and the co-occurrence of Ca and Zr in some analyses suggests the presence of zirconolite [$CaZrTi_2O_7$]. In

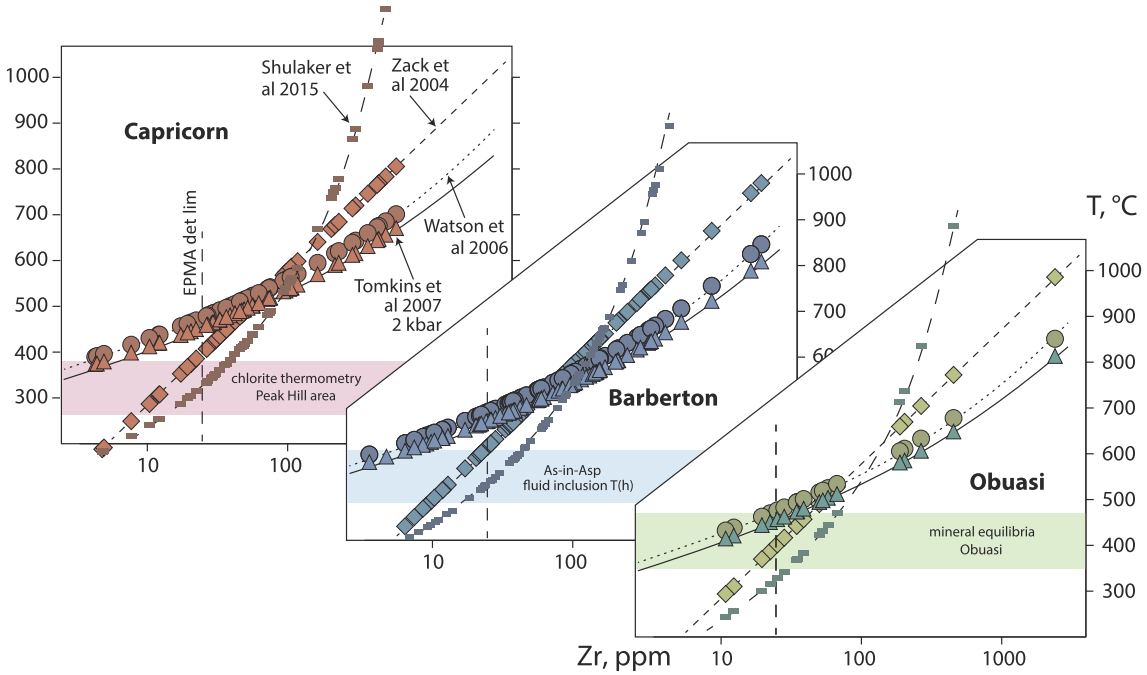

Fig. 8. Estimates of crystallisation temperature based on Zr-in-rutile geothermometry compared with independent geothermometric methods (shaded areas, see Supplementary Material for details). Zirconium-in-rutile calibrations of Shulaker et al. (2015), Tomkins et al. (2007), Watson et al. (2006), Zack et al. (2004).

addition to nanoinclusions, excess Zr may have been incorporated during fast crystal growth.

5.4. Fluid transport and metal availability in orogenic gold deposits

Antimony is common in the mesozonal to epizonal portions (< 10 km depth) of orogenic gold deposits (Goldfarb and Groves, 2015), and Sb-bearing sulfides, such as ullmannite and tetrahedrite, are known in gold deposits of the Barberton Greenstone Belt and the Ashanti Belt (Agangi et al., 2014). Anomalously high concentrations of Sb, as well as Au, As, Ag, V, W, Te, and Hg in orogenic gold deposits relative to average crustal values (Goldfarb and Groves, 2015) can be explained by remobilisation during metamorphism at greenschist and amphibolite facies conditions due to chlorite dehydration and conversion of pyrite to pyrrhotite (Finch and Tomkins, 2017; Pitcairn et al., 2015). Transport of many of these elements in these deposits is believed to be a consequence of the low-salinity aqueo-carbonic nature of mineralising fluids. In these fluids, gold is thought to be transported by hydrosulfide complexes such as $Au(HS)^{2-}$ and AuHS (Pokrovski et al., 2014). Other cations that have an affinity for reduced S, such as As and Sb, are also transported by the same fluids (as SbS^{2-}, SbS_3^{3-}, SbS_4^{3-}, $SbS(HS)_3$, $Sb(HS)^{4+}$) (Sherman et al., 2000). Low fluid salinities cause low solubility levels of all cations forming Cl complexes, such as base metals, resulting in the high Au/metal ratios that are typical of orogenic gold deposits.

However, the enrichment in Nb, Ta and to a lesser extent W in our rutile analyses is not explained by the presence of S in the fluid. Instead, these high field-strength cations (5+ and 6+) form complexes with F in aqueous fluids, and tend to be enriched in rocks formed from strongly fractionated, typically F-rich and high-F/Cl felsic magmas, such as pegmatites and associated hydrothermal fluids (Agangi et al., 2012; Carruzzo et al., 2006; Chevychelov et al., 2005). In these igneous rocks and magmatic-hydrothermal deposits, enrichment in Sn, Zr and other high field-strength elements to form economically viable tantalite-columbite-ixiolite-tapiolite minerals is well known (Černý et al., 1999; Sanematsu et al., 2016). The occurrence of F-bearing phases in our samples, such as fluorapatite, indicates the presence of F in the mineralising fluids (Fig. 2), offering an explanation for the mobilisation of high field strength elements. In addition to F, the carbonate ion $[CO_3^{2-}]$ may have also contributed to the transport of these elements (Pokrovski et al., 2014). Thus, mineralising fluids in orogenic gold deposits are complex fluids that are capable of mobilising relatively insoluble high field-strength elements, a characteristic that is instrumental in the formation of rutile.

6. Concluding remarks

Analysis of rutile from three orogenic gold provinces formed at similar greenschist facies conditions demonstrate that the chemical composition of rutile can be used to discriminate between gold-mineralised rocks and other types of non-mineralised rocks of various petrogenetic origins. Our results indicate that trace element composition of rutile, primarily the Sb content, in combination with other elements, such as W and V, offer the best indications of orogenic gold mineralisation. Estimates of rutile crystallisation temperature based on the Zr content of hydrothermal rutile may not reflect equilibrium conditions and should be used with care; the presence of Zr-bearing inclusions should be evaluated. The results of this study of hydrothermal rutile can also be applied to the study of detrital rutile, and in particular to greenfield exploration of orogenic Au deposits. The study of detrital rutile can aid in identifying the source rocks, including mafic vs felsic derivation (based on Cr-Nb), association with evolved granitoids and related hydrothermal deposits (Nb, W and Sn) and association with gold deposits (Sb in particular).

Acknowledgments

This research was funded by the Science and Industry Endowment Fund (SIEF) as part of The Distal Footprints of Giant Ore Systems: UNCOVER Australia Project (RP04-063) — Capricorn Distal Footprints, Australia. C. Rippon of Sheba Mines is thanked for providing some of the samples for this study. B. McDonald is thanked for assistance with LA-ICP-MS analyses.

Appendix A. Supplementary data

Supplementary data to this article can be found online at https://doi.org/10.1016/j.oregeorev.2019.01.018.

References

Agangi, A., Hofmann, A., Eickmann, B., Marin-Carbonne, J., Reddy, S.M., 2016. An atmospheric source of S in Mesoarchaean structurally-controlled gold mineralisation of the Barberton Greenstone Belt. Precambr. Res. 285, 10–20.

Agangi, A., Hofmann, A., Przybyłowicz, W., 2014. Trace element zoning of sulfides and quartz at Sheba and Fairview gold mines: clues to Mesoarchean mineralisation in the Barberton Greenstone Belt, South Africa. Ore Geol. Rev. 56, 94–114.

Agangi, A., Kamenetsky, V.S., McPhie, J., 2012. Evolution and emplacement of high fluorine rhyolites in the Mesoproterozoic Gawler silicic large igneous province, South Australia. Precambrian Res. 208–211, 124–144.

Anhaeusser, C.R., 1973. The evolution of the early Precambrian crust of southern Africa. Philos. Trans. R. Soc. London A 273, 359–388.

Anhaeusser, C.R., 1986. Archaean gold mineralization in the Barberton Mountain Land. In: In: Anhaeusser, C.R., Maske, S. (Eds.), Mineral Deposits of Southern Africa Vol. I. Geol, Soc. South Africa, pp. 113–154.

Armstrong, J.T., 1988. Quantitative analysis of silicates and oxide minerals: comparison of Monte-Carlo, ZAF and Phi-Rho-Z procedures. Microbeam Anal. 239–246.

Belousova, E.A., Griffin, W.L., O'Reilly, S.Y., Fisher, N.I., 2002. Apatite as an indicator mineral for mineral exploration: trace-element compositions and their relationship to host rock type. J. Geochem. Explor. 76, 45–69.

Cabral, A.R., Eugster, O., Brauns, M., Lehmann, B., Rösel, D., Zack, T., de Abreu, F.R., Pernicka, E., Barth, M., 2013. Direct dating of gold by radiogenic helium: testing the method on gold from Diamantina, Minas Gerais, Brazil. Geology 41, 163–166.

Cabral, A.R., Rios, F.J., de Oliveira, L.A.R., de Abreu, F.R., Lehmann, B., Zack, T., Laufek, F., 2015. Fluid-inclusion microthermometry and the Zr-in-rutile thermometer for hydrothermal rutile. Int. J. Earth Sci. 104, 513–519.

Cabri, L.J., Chryssoulis, S.L., de Villiers, J.P.R., Laflamme, J.H.G., Buseck, P.R., 1989. The nature of "invisible" gold in arsenopyrite. Canadian Mineral. 27, 353–362.

Cao, M., Li, G., Qin, K., Seitmuratova, E.Y., Liu, Y., 2012. Major and trace element characteristics of apatite in granitoids from central Kazakhstan: implications for petrogenesis and mineralisation. Resour. Geol. 62, 63–83.

Carruzzo, S., Clarke, D.B., Pelrine, K.M., MacDonald, M.A., 2006. Texture, composition, and origin of rutile in the South Mountain Batholith, Nova Scotia. Canadian Mineral. 44, 715–729.

Cave, B.J., Stepanov, A.S., Craw, D., Large, R.R., Halpin, J.A., Thompson, J., 2015. Release of trace elements through the sub-greenschist facies breakdown of detrital rutile to metamorphic titanite in the Otago Schist, New Zealand. Canadian Mineral. 53, 379–400.

Černý, P., Chapman, R., Simmons, W.B., Chackowsky, L.E., 1999. Niobian rutile from the McGuire granitic pegmatite, Park County, Colorado; solid solution, exsolution, and oxidation. Am. Mineral. 84, 754–763.

Chevychelov, V.Y., Zaraisky, G.P., Borisovskii, S.E., Borkov, D.A., 2005. Effect of melt composition and temperature on the partitioning of Ta, Nb, Mn, and F between granitic (alkaline) melt and fluorine-bearing aqueous fluid: fractionation of Ta and Nb and conditions of ore formation in rare-metal granites. Petrology 13, 305–321.

Clark, J. R., and Williams-Jones, A. E., 2004, Rutile as a potential indicator mineral for metamorphosed metallic ore deposits, Rapport Final de DIVEX, Sous-projet SC2: Montreal, p. 17.

de Ronde, C.E.J., Kamo, S.L., 2000. An Archaean arc-arc collisional event: a short-lived (ca 3 Myr) episode, Weltevreden area, Barberton greenstone belt, South Africa. J. Afr. Earth Sci. 30, 219–248.

de Ronde, C.E.J., Spooner, E.T.C., de Wit, M.J., Bray, C.J., 1992. Shear zone-related, Au quartz vein deposits in the Barberton greenstone belt, South Africa; field and petrographic characteristics, fluid properties, and light stable isotope geochemistry. Econ. Geol. 87, 366–402.

Diener, J.F.A., Stevens, G., Kisters, A.F.M., Poujol, M., 2005. Metamorphism and exhumation of the basal parts of the Barberton greenstone belt, South Africa: constraining the rates of Mesoarchaean tectonism. Precambr. Res. 143, 87–112.

Dirks, P.H.G.M., Charlesworth, E.G., Munyai, M.R., Wormald, R., 2013. Stress analysis, post-orogenic extension and 3.01 Ga gold mineralisation in the Barberton Greenstone Belt, South Africa. Precambrian Res. 226, 157–184.

Donovan, J.J., Tingle, T.N., 1996. An improved mean atomic number background correction for quantitative microanalysis. Microbeam Analysis 2, 1–7.

Donovan, J.J., Snyder, D.A., Rivers, M.L., 1993. An improved interference correction for trace element analysis. Microbeam Analysis v, 2.

Dostal, J., Kontak, D.J., Chatterjee, A.K., 2009. Trace element geochemistry of scheelite and rutile from metaturbidite-hosted quartz vein gold deposits, Meguma Terrane, Nova Scotia, Canada. Genetic Implicat.: Mineral. Petrol. 97, 95–109.

Dziggel, A., Armstrong, R.A., Stevens, G., Nasdala, L., 2005. Growth of zircon and titanite during metamorphism in the granitoid-gneiss terrane south of the Barberton greenstone belt, South Africa. Mineral. Mag. 69, 1019–1036.

Dziggel, A., Poujol, M., Otto, A., Kisters, A.F.M., Trieloff, M., Schwarz, W.H., Meyer, F.M., 2010. New U-Pb and $^{40}Ar/^{39}Ar$ ages from the northern margin of the Barberton greenstone belt, South Africa: implications for the formation of Mesoarchaean gold deposits. Precambr. Res. 179, 206–220.

Finch, E.G., Tomkins, A.G., 2017. Pyrite-pyrrhotite stability in a metamorphic aureole: implications for orogenic gold genesis. Econ. Geol. 112, 661–674.

Force, E.R., 1980. The provenance of rutile. J. Sediment. Res. 50, 485–488.

Fougerouse, D., Micklethwaite, S., Tomkins, A.G., Mei, Y., Kilburn, M., Guagliardo, P., Fisher, L.A., Halfpenny, A., Gee, M., Paterson, D., Howard, D.L., 2016a. Gold remobilisation and formation of high grade ore shoots driven by dissolution-reprecipitation replacement and Ni substitution into auriferous arsenopyrite. Geochim. Cosmochim. Acta 178, 143–159.

Fougerouse, D., Micklethwaite, S., Ulrich, S., Miller, J., Godel, B., Adams, D.T., McCuaig, T.C., 2016b. Evidence for two stages of mineralisation in west Africa's largest gold deposit: Obuasi, Ghana. Econ. Geol. 111, 3–22.

Fougerouse, D., Reddy, S.M., Saxey, D.W., Rickard, W.D.A., van Riessen, A., Micklethwaite, S., 2016c. Nanoscale gold clusters in arsenopyrite controlled by growth rate not concentration: Evidence from atom probe microscopy. Am. Mineral. 101, 1916–1919.

Frimmel, H.E., 2008. Earth's continental crustal gold endowment. Earth Planet. Sci. Lett. 267, 45–55.

Goldfarb, R.J., Groves, D.I., 2015. Orogenic gold: common or evolving fluid and metal sources through time. Lithos 233, 2–26.

Harris, D. C., 1989, The Mineralogy and Geochemistry of the Hemlo Gold Deposit, Ontario, in Canada, G.S.o., ed., 38, p. 88.

Hawke, M. L., Davidson, G. J., Meffre, S., Hilliard, P., Large, R., and Gemmell, J. B., 2015, Geological Evolution of the DeGrussa Cu-Au-Ag Volcanic-Hosted Massive Sulfide Deposit, Western Australia: SEG 2015, Hobart, TAS, 27-30 September 2015, 2015.

Herrington, R., 2013. Road map to mineral supply. Nat. Geosci. 6, 892–894.

Jiang, Z., Oliver, N.H.S., Barr, T.D., Power, W.L., Ord, A., 1997. Numerical modeling of fault-controlled fluid flow in the genesis of tin deposits of the Malage ore field, Gejiu mining district, China. Econ. Geol. 92, 228–247.

John, T., Klemd, R., Hirdes, W., Loh, G., 1999. The metamorphic evolution of the Paleoproterozoic (Birimian) volcanic Ashanti belt (Ghana, West Africa). Precambr. Res. 98, 11–30.

Kamo, S.L., Davis, D.W., 1994. Reassessment of Archean crustal development in the Barberton Mountain Land, South Africa, based on U-Pb dating. Tectonics 13, 167–192.

Kotková, J., Harley, S.L., 2010. Anatexis during high-pressure crustal metamorphism: evidence from garnet–whole-rock REE relationships and zircon–rutile Ti–Zr thermometry in leucogranulites from the Bohemian Massif. J. Petrol. 51, 1967–2001.

Liou, J.G., Zhang, R., Ernst, W.G., Liu, J., McLimans, R., 1998. Mineral parageneses in the Piampaludo eclogitic body, Gruppo di Voltri, western Ligurian Alps. Schweiz. Mineral. Petrogr. Mitt. 78, 317–335.

Liu, L., Xiao, Y., Wörner, G., Kronz, A., Simon, K., Hou, Z., 2014. Detrital rutile geochemistry and thermometry from the Dabie orogen: implications for source–sediment links in a UHPM terrane. J. Asian Earth Sci. 89, 123–140.

Luvizotto, G.L., Zack, T., 2009. Nb and Zr behavior in rutile during high-grade metamorphism and retrogression: an example from the Ivrea-Verbano Zone. Chem. Geol. 261, 303–317.

Mao, M., Rukhlov, A.S., Rowins, S.M., Spence, J., Coogan, L.A., 2016. Apatite trace element compositions: a robust new tool for mineral exploration. Econ. Geol. 111, 1187–1222.

Meinhold, G., Anders, B., Kostopoulos, D., Reischmann, T., 2008. Rutile chemistry and thermometry as provenance indicator: an example from Chios Island, Greece. Sed. Geol. 203, 98–111.

Mikucki, E.J., Ridley, J.R., 1993. The hydrothermal fluid of Archaean lode-gold deposits at different metamorphic grades: compositional constraints from ore and wallrock alteration assemblages. Miner. Deposita 28, 469–481.

Morad, S., 1986. SEM study of authigenic rutile, anatase and brookite in Proterozoic sandstones from Sweden. Sed. Geol. 46, 77–89.

Mumin, A.H., Fleet, M.E., Chryssoulis, S.L., 1994. Gold mineralization in As-rich mesothermal gold ores of the Bogosu-Prestea mining district of the Ashanti Gold Belt, Ghana: remobilization of "invisible" gold. Miner. Deposita 29, 445–460.

Mumin, A.H., Fleet, M.E., 1995. Evolution of gold mineralization in the Ashanti Gold Belt, Ghana: evidence from carbonate compositions and parageneses. Mineral. Petrol. 55, 265–280.

Myers, J.S., Shaw, R.D., Tyler, I.M., 1996. Tectonic evolution of Proterozoic Australia. Tectonics v. 15, 1431–1446.

Oberthür, T., Vetter, U., Davis, D.W., Amanor, J.A., 1998. Age constraints on gold mineralization and Paleoproterozoic crustal evolution in the Ashanti belt of southern Ghana. Precambr. Res. 89, 129–143.

Occhipinti, S.A., Sheppard, S., Passchier, C., Tyler, I.M., Nelson, D.R., 2004. Palaeoproterozoic crustal accretion and collision in the southern Capricorn Orogen: the Glenburgh Orogeny. Precambr. Res. 128, 237–255.

Pape, J., Mezger, K., Robyr, M., 2016. A systematic evaluation of the Zr-in-rutile thermometer in ultra-high temperature (UHT) rocks. Contrib. Miner. Petrol. 171, 1–20.

Perrouty, S., Aillères, L., Jessell, M.W., Baratoux, L., Bourassa, Y., Crawford, B., 2012. Revised Eburnean geodynamic evolution of the gold-rich southern Ashanti Belt, Ghana, with new field and geophysical evidence of pre-Tarkwaian deformations. Precambr. Res. 204–205, 12–39.

Pirajno, F., 2004. Metallogeny in the Capricorn Orogen, Western Australia, the result of multiple ore-forming processes. Precambr. Res. 128, 411–439.

Pirajno, F., Occhipinti, S.A., Swager, C.P., 2000. Geology and Mineralisation of the Palaeoproterozoic Bryah and Padbury basins Western Australia. Geological Survey of Western Australia Department of Minerals and Energy, pp. 52 59.

Pitcairn, I., Craw, D., Teagle, D.H., 2015. Metabasalts as sources of metals in orogenic gold deposits. Miner. Deposita 50, 373–390.

Plavsa, D., Reddy, S.M., Agangi, A., Clark, C., Kylander-Clark, A., Tiddy, C.J., 2018. Microstructural, trace element and geochronological characterisation of TiO_2 polymorphs and implications for mineral exploration. Chem. Geol. 476, 130–149.

Pochon, A., Beaudoin, G., Branquet, Y., Boulvaisa, P., Gloaguenc, E., Gapaisa, D., 2017. Metal mobility during hydrothermal breakdown of Fe-Ti oxides: Insights from Sb-Au

mineralizing event (Variscan Armorican Massif, France). Ore Geol. Rev. 91, 66–99.
Pokrovski, G.S., Akinfiev, N.N., Borisova, A.Y., Zotov, A.V., Kouzmanov, K., 2014. Gold speciation and transport in geological fluids: insights from experiments and physical-chemical modelling. Geol. Soc. Spec. Pub. 402, 9–70.
Putnis, A., 1978. The mechanism of exsolution of hematite from iron-bearing rutile. Phys. Chem. Miner. v. 3, 183–197.
Rabbia, O.M., Hernández, L.B., French, D.H., King, R.W., Ayers, J.C., 2009. The El Teniente porphyry Cu-Mo deposit from a hydrothermal rutile perspective. Miner. Deposita 44, 849–866.
Reddy, S.M., Timms, N.E., Pantleon, W., Trimby, P., 2007. Quantitative characterization of plastic deformation of zircon and geological implications. Contrib. Miner. Petrol. 153, 625–645.
Rice, C.M., Darke, K.E., Still, J.W., Lachowski, E.E., 1998. Tungsten-bearing rutile from the Kori Kollo gold mine, Bolivia. Mineral. Mag. 62, 421–429.
Sanematsu, K., Ejima, T., Kon, Y., Manaka, T., Zaw, K., Morita, S., Seo, Y., 2016. Fractionation of rare-earth elements during magmatic differentiation and weathering of calc-alkaline granites in southern Myanmar. Mineral. Mag. 80, 77–102.
Schoene, B., de Wit, M.J., Bowring, S.A., 2008. Mesoarchean assembly and stabilization of the eastern Kaapvaal craton: a structural-thermochronological perspective. Tectonics 27, p. TC5010.
Schwartz, M.O., Oberthuer, T., Amanor, J., Gyapong, W.A., 1992. Fluid inclusion re-equilibration and P-T-X constraints on fluid evolution in the Ashanti gold deposit, Ghana. Eur. J. Mineral. 4, 1017–1033.
Scott, K.M., 2005. Rutile geochemistry as a guide to porphyry Cu–Au mineralisation, Northparkes, New South Wales, Australia. Geochem. Explor. Environ. Anal. 5, 247–253.
Scott, K.M., Radford, N.W., 2007. Rutile compositions at the Big Bell Au deposit as a guide for exploration. Geochem.: Explor. Environ., Anal. 7, 353–361.
Sherman, D.M., Ragnarsdottir, K.V., Oelkers, E.H., 2000. Antimony transport in hydrothermal solutions: an EXAFS study of antimony(V) complexation in alkaline sulfide and sulfide–chloride brines at temperatures from 25 °C to 300 °C at Psat. Chem. Geol. 167, 161–167.
Shulaker, D.Z., Schmitt, A.K., Zack, T., Bindeman, I., 2015. In-situ oxygen isotope and trace element geothermometry of rutilated quartz from Alpine fissures. Am. Mineral. 100, 915–925.
Sibson, R.H., Robert, F., Poulsen, K.H., 1988. High-angle reverse faults, fluid-pressure cycling, and mesothermal gold-quartz deposits. Geology 16, 551–555.
Shannon, R.D., 1976. Revised effective ionic radii and systematic studies of interatomic distances in halides and chalcogenides. Acta Crystallogr. A 32, 751–767. https://doi.org/10.1107/S0567739476001551.
Skublov, S.G., Zack, T., Berezin, A.V., Mel'nik, A.E., Rizvanova, N.G., 2013. In situ LA-ICP-MS investigation of the geochemistry and U-Pb age of rutile from the rocks of the Belomorian mobile belt. Geochem. Int. 51, 164–171.
Smith, D.C., Perseil, E.A., 1997. Sb-rich rutile in the manganese concentrations St. Marcel-Praborna, Aosta Valley, Italy: petrology and crystal-chemistry. Mineral. Mag. 61, 655–669.
Stacey, J.S., Kramers, J.D., 1975. Approximation of terrestrial lead isotope evolution by a two-stage model. Earth Planet. Sci. Lett. 26, 207–221.
Taylor, R., Clark, C., Reddy, S.M., 2012. The effect of grain orientation on secondary ion mass spectrometry (SIMS) analysis of rutile. Chem. Geol. 300–301, 81–87.
Thornett, S., 1995. The Nature and Timing of Gold Mineralisation in the Proterozoic Rocks of the Peak Hill Schist District. University of Western Australia, pp. 155.
Tomkins, H.S., Powell, R., Ellis, D.J., 2007. The pressure dependence of the zirconium-in-rutile thermometer. J. Metamorph. Geol. 25, 703–713.
Triebold, S., Luvizotto, G.L., Tolosana-delgado, R., Zack, T., von Eynatten, H., 2011. Discrimination of TiO_2 polymorphs in sedimentary and metamorphic rocks. Contrib. Miner. Petrol. 161, 581–596.
Verberne, R., Reddy, S.M., Saxey, D.W., Rickard, W.D.A., Fougerouse, D., Plavsa, D., Agangi, A, 2017. Trace element nanoclusters in natural rutile (TiO_2) and their geological significance. In: 5th Australian Atom Probe Workshop, Magnetic Island, Australia, June.
Viljoen, M.J., Viljoen, R.P., 1969, Introduction to the geology of the Barberton granite-greenstone terrain: Geological Society of South Africa Special Publication, vol. 2, p. 9–28.
Vry, J.K., Baker, J.A., 2006. LA-MC-ICPMS Pb–Pb dating of rutile from slowly cooled granulites: confirmation of the high closure temperature for Pb diffusion in rutile. Geochim. Cosmochim. Acta 70, 1807–1820.
Watson, E.B., Wark, D.A., Thomas, J.B., 2006. Crystallisation thermometers for zircon and rutile. Contrib. Miner. Petrol. 151, 413–433.
Wilson, A.W., Cesbron, F., 1977. Rutile and apatite: useful prospecting guides for porphyry copper deposits. Mineral. Mag. 41, 288–292.
Windh, J., 1992. Tectonic Evolution and Metallogenesis of the Early Proterozoic Glengarry Basin (Ph.D thesis). University of Western Australia, Western Australia.
Yang, H.Y., 1987. Stability of ilmenite and titanomagnetite in the presence of carbon dioxide – a thermodynamic evaluation. Contrib. Miner. Petrol. 95, 202–206.
Zack, T., Kronz, A., Foley, S.F., Rivers, T., 2002. Trace element abundances in rutiles from eclogites and associated garnet mica schists. Chem. Geol. 184, 97–122.
Zack, T., Moraes, R., Kronz, A., 2004. Temperature dependence of Zr in rutile: Empirical calibration of a rutile thermometer. Contrib. Miner. Petrol. 148, 471–488.